RESEARCH ARTICLE

Efficient estimation of propagator anisotropy and non-Gaussianity in multishell diffusion MRI with micro-structure adaptive convolution kernels and dual Fourier integral transforms

Guillem París[1] | Tomasz Pieciak[1,2] | Santiago Aja-Fernández[1] | Antonio Tristán-Vega[1]

[1]Laboratorio de Procesado de Imagen (LPI), Universidad de Valladolid, Valladolid, Castilla y León Spain

[2]AGH University of Science and Technology, Krakow, Poland

Correspondence
Guillem París, Laboratorio de Procesado de Imagen (LPI), Universidad de Valladolid, Valladolid, Spain.
Email: guillem.paris@uva.es

Purpose: We seek to reformulate the so-called Propagator Anisotropy (PA) and Non-Gaussianity (NG), originally conceived for the Mean Apparent Propagator diffusion MRI (MAP-MRI), to the Micro-Structure adaptive convolution kernels and dual Fourier Integral Transforms (MiSFIT). These measures describe relevant normalized features of the Ensemble Average Propagator (EAP).

Theory and Methods: First, the indices, which are defined as the EAP's dissimilarity from an isotropic (PA) or a Gaussian (NG) one, are analytically reformulated within the MiSFIT framework. Then a comparison between the resulting maps is drawn by means of a visual analysis, a quantitative assessment via numerical simulations, a test-retest study across the MICRA dataset (6 subjects scanned five times) and, finally, a computational time evaluation.

Results: Findings illustrate the visual similarity between the indices computed with either technique. Evaluation against synthetic ground truth data, however, demonstrates MiSFIT's improved accuracy. In addition, the test–retest study reveals MiSFIT's higher degree of reliability in most of white matter regions. Finally, the computational time evaluation shows MiSFIT's time reduction up to two orders of magnitude.

Conclusions: Despite being a direct development on the MAP-MRI representation, the PA and the NG can be reliably and efficiently computed within MiSFIT's framework. This, together with the previous findings in the original MiSFIT's article, could mean the difference that definitely qualifies diffusion MRI to be incorporated into regular clinical settings.

KEYWORDS
anisotropy, EAP, MiSFIT, multishell, non-Gaussianity, propagator

1 | INTRODUCTION

Diffusion MRI (dMRI) has become an irreplaceable tool for the noninvasive study of the micro- and meso-structure of the white matter (WM) of the brain. While the micro-structure is usually characterized through suitable diffusion models, the description of the meso-structure entails the reconstruction and analysis of the Ensemble Average Propagator (EAP),[1] defined as the Probability Density Function of water molecules moving a distance **R** within a diffusion time τ.[2] The topic covered in this paper focuses on the latter. Specifically, we address the characterization of the three-dimensional EAP computed from multi-shell samplings, that is, dMRI acquisitions comprising a *small* set of b-values (shells) with a *large* number of diffusion gradients each.[3]

Reconstructing the three-dimensional EAP allows to compute several scalar indices that embed useful descriptors of WM. Among them, return-to-origin, return-to-plane or return-to-axis probabilities (respectively, RTOP, RTPP, and RTAP), as well as propagator anisotropy (PA) or non-Gaussianity (NG) are the most often used.[4-6] In the present paper we focus on PA and NG, which come to generalize the popular Fractional Anisotropy (FA) and diffusion Kurtosis.

PA is defined in Reference 6 as the distance from the propagator $P(\mathbf{R})$ to its isotropic equivalent. By means of Parseval's theorem, it can also be defined as the distance from the attenuation signal $E(\mathbf{q})$ (the diffusion signal characterized by wave vector $\mathbf{q}$ over the unweighted T2 baseline) to its closest isotropic counterpart, $O(\mathbf{q})$:

$$PA = \gamma(\sin(\angle(E(\mathbf{q}), O(\mathbf{q}))), \varepsilon) \in [0, 1], \quad (1)$$

where:

$$\cos(\angle(E(\mathbf{q}), O(\mathbf{q}))) = \frac{\langle E(\mathbf{q}), O(\mathbf{q}) \rangle}{\|E(\mathbf{q})\| \|O(\mathbf{q})\|}, \quad (2)$$

and:

$$\gamma(t, \varepsilon) = \frac{t^{3\varepsilon}}{1 - 3t^{\varepsilon} + 3t^{2\varepsilon}}, \quad (3)$$

for $\varepsilon = 0.4$, which stands for a contrast enhancement of PA within the normalized range $[0, 1]$. PA has shown the ability to characterize morphological and cytoarchitectural attributes, even in Gray Matter regions where the FA is non-informative.[7] Yet, PA offers a more accurate assessment of the anisotropic behavior in crossing fibers regions. Within clinical setups, PA has shown a great potential in the analysis of longitudinal changes within subjects,[8] the characterization of cognitive impairment after traumatic brain injury[9] impaired social cognition in autism,[10] or

age-dependent neuronal demise in transgenic Alzheimer rats.[11]

In turn, NG is defined as the distance from $E(\mathbf{q})$ to its closest Gaussian representation, $G(\mathbf{q})$:[6]

$$NG = \sin(\angle(E(\mathbf{q}), G(\mathbf{q}))) \in [0, 1]. \quad (4)$$

Though the clinical applicability of NG has not been as thoroughly tested as that of PA, it has been lately proven useful at distinguishing grade II from grade III and IV gliomas,[12] relevant for the noninvasive preoperative evaluation of tumour pathological grading. Some additional studies on axonal loss and demyelination,[13] as well as head and neck cancer[14,15] are also available.

Though they can be computed resorting to other estimation techniques,[5] PA and NG naturally arise from MAP-MRI.[4,6] Therein, the NG can be easily computed from the energy of the non-DC components, since MAP-MRI develops the diffusion signal by successively refining a Gaussian model. Conversely, the PA is related to the non-DC components of the isotropic, non-voxel adaptive version of MAP-MRI, a.k.a. 3D-SHORE.

In this article, we aim at formulating and evaluating both PA and NG for the newly developed Micro-Structure adaptive convolution kernels and dual Fourier Integral Transforms (MiSFIT[16]), both of them from the very same signal representation. By taking advantage of the computational efficiency of MISFIT, we expect the already-demonstrated higher accuracy in the RTxP computation w.r.t MAPL (the de facto standard, regularized version of MAP-MRI[4]) to also be translated for PA and NG. In addition, we also expect this accuracy to result in a higher reliability of the measures, which together with the critical reduction of the computational time, qualify MiS-FIT's PA and NG to be incorporated not only in research studies, but also in clinical settings.

2 | THEORY

2.1 | MiSFIT's signal representation

MiSFIT's composite representation, as it can be seen in Reference 16 equation (4), comprises the aggregate of a free-diffusing isotropic component and a semi-parametric component that accounts for the partial volume fraction $f \in [0, 1]$ of constrained diffusion:

$$_c E(\mathbf{q}) = (1 - f) \exp(-bD_0) + fE(\mathbf{q}), \quad (5)$$

with $\mathbf{q} = q\mathbf{u}$ ($q = \|\mathbf{q}\| \in \mathbb{R}_+$) the wave-vector related to the b-value as $b = 4\pi^2 \tau q^2$ and D_0 the diffusivity of free-water at body temperature. The constrained diffusion signal $E(\mathbf{q})$

is drawn as the spherical convolution of a parametric kernel, defined by the longitudinal $\lambda_\parallel$ and transverse $\lambda_\perp$ diffusivities, with a nonparametric orientation distribution Function (ODF), Φ:

$$E(\mathbf{q}) = \iint_S \Phi(\mathbf{v}) \exp\left(-b\left((\mathbf{u}^T\mathbf{v})(\lambda_\parallel - \lambda_\perp) + \lambda_\parallel\right)\right) d\mathbf{v}, \quad (6)$$

where $S = \{\mathbf{u} \in \mathbb{R}^3 : \|\mathbf{u}\| = 1\}$. By representing the ODF in the basis of Spherical Harmonics (SH), MiSFIT lastly represents the attenuation signal as:

$$E(q\mathbf{u}) = \sum_{\substack{l=0 \\ l \text{ even}}}^{L} \sum_{m=-l}^{l} \hat{e}_l^{\text{ODF}}(q)\phi_l^m Y_l^m(\mathbf{u}), \quad (7)$$

where $Y_l^m(\mathbf{u})$ are the (even) SH functions, ϕ_l^m stand for the SH coefficients of the ODF, and $\hat{e}_l^{\text{ODF}}(q)$ are $\lambda_\parallel$ and $\lambda_\perp$-dependent convolution multipliers (see Reference 16 for further details). A central part to our developments, as can be easily deduced from Equations (1) and (4), is the computation of scalar products between SH-spanned functions like in Equation (7). We prove in Supporting Information Appendix A that their calculation relies on the evaluation of the following integral, $\mathcal{I}_l(\rho_\lambda)$, involving the Legendre Polynomials $P_l(x_i)$:

$$\mathcal{I}_l(\rho_\lambda) = \iint_{-1}^{1} \frac{P_l(x_1)P_l(x_2)}{(2\rho_\lambda + x_1^2 + x_2^2)^{3/2}} dx_1 dx_2, \quad (8)$$

for $\rho_\lambda = \lambda_\perp/(\lambda_\parallel - \lambda_\perp)$. These integrals do not admit a closed form. However, since only the first few even orders of l are needed, they can be precomputed for a wide range of ρ_λ and with an accuracy up to the numerical precision of the machine. Figure 1 shows their values for the first few l.

2.2 | PA for MiSFIT's composite signal

From the definition in Equation (1), we develop into:

$$\sin\left(\angle(_cE(\mathbf{q}), _cO(\mathbf{q}))\right) = \sqrt{1 - \cos^2\left(\angle(_cE(\mathbf{q}), _cO(\mathbf{q}))\right)}. \quad (9)$$

We demonstrate in Supporting Information Appendix B that the squared cosine in the last equation leads to:

$$\cos^2\left(\angle(_cE(\mathbf{q}), cO(\mathbf{q}))\right)$$
$$= \frac{\|_cO(q)\|^2}{\|_cE(q\mathbf{u})\|^2} = \frac{(1-f)^2O_{\text{iso}} + f^2O_{\text{ani}} + f(1-f)O_{\text{mix}}}{(1-f)^2E_{\text{iso}} + f^2E_{\text{ani}} + f(1-f)E_{\text{mix}}}, \quad (10)$$

where the isotropic terms (E_{iso}, O_{iso}), the anisotropic terms (E_{ani}, O_{ani}), and the mixed terms (E_{mix}, O_{mix}) come

from the composite representation (i.e., isotropic plus anisotropic parts) in Equation (5):

$$O_{\text{ani}} = (\phi_0^0)^2 \pi \delta_\lambda^{-3/2} \mathcal{I}_0(\rho_\lambda);$$
$$E_{\text{ani}} = \sum_{l,m} (\phi_l^m)^2 \pi \delta_\lambda^{-3/2} \mathcal{I}_l(\rho_\lambda); \quad (11)$$

$$E_{\text{iso}} = O_{\text{iso}} = (2D_0)^{-3/2};$$
$$E_{\text{mix}} = O_{\text{mix}} = 4\sqrt{\pi}\phi_0^0\left((D_0 + \lambda_\perp)\sqrt{D_0 + \lambda_\parallel}\right)^{-1}, \quad (12)$$

for $\delta_\lambda = \lambda_\parallel - \lambda_\perp$. Therefore, the PA finally reads:

$$\text{PA} = \gamma\left(\sqrt{1 - \frac{\frac{(1-f)^2}{(2D_0)^{3/2}} + \frac{4\sqrt{\pi}f(1-f)}{(D_0+\lambda_\perp)\sqrt{D_0+\lambda_\parallel}}\phi_0^0 + f^2(\phi_0^0)^2\pi\delta_\lambda^{-3/2}\mathcal{I}_0(\rho_\lambda)}{\frac{(1-f)^2}{(2D_0)^{3/2}} + \frac{4\sqrt{\pi}f(1-f)}{(D_0+\lambda_\perp)\sqrt{D_0+\lambda_\parallel}}\phi_0^0 + f^2\sum_{l,m}(\phi_l^m)^2\pi\delta_\lambda^{-3/2}\mathcal{I}_l(\rho_\lambda)}}, \varepsilon\right). \quad (13)$$

Noticeably, removing the isotropic compartment (i.e., taking $f = 1$) results in a much simpler expression:

$$\text{PA} = \gamma\left(\sqrt{1 - \frac{O_{\text{ani}}}{E_{\text{ani}}}}, \varepsilon\right)$$
$$= \gamma\left(\sqrt{1 - \frac{(\phi_0^0)^2\pi\delta_\lambda^{-3/2}\mathcal{I}_0(\rho_\lambda)}{\sum_{l,m}(\phi_l^m)^2\pi\delta_\lambda^{-3/2}\mathcal{I}_l(\rho_\lambda)}}, \varepsilon\right). \quad (14)$$

Conversely, fitting a voxel with $f = 0$ (i.e., a free-water voxel), results in both $\|_cO(q)\|^2$ and $\|_cE(q\mathbf{u})\|^2$ being equal. Hence, the PA as defined in Equation (9), will be 0 as expected.

2.3 | NG for MiSFIT's composite signal

Now, from the definition in Equation (4):

$$\sin(\angle(_cE(\mathbf{q}), _cG(\mathbf{q}, \hat{\mathbf{D}}))) = \sqrt{1 - \left(\frac{\langle _cE(\mathbf{q}), _cG(\mathbf{q}, \hat{\mathbf{D}})\rangle}{\|_cE(\mathbf{q})\|\|_cG(\mathbf{q}, \hat{\mathbf{D}})\|}\right)^2}, \quad (15)$$

where $_cG(\mathbf{q}, \hat{\mathbf{D}})$ is the closest Gaussian propagator. In the MiSFIT approach, the equivalent Gaussian propagator is estimated by fitting a tensor to the EAP-based reconstruction of the attenuation signal (for b-values < 2000 s/mm^2). The reason behind this is that computing the actual closest Gaussian propagator (i.e. that which results in the smallest possible Mean Squared Difference) is not trivial and would require solving a calculus of variations problem that could easily maim the computational efficiency nature upon which MiSFIT is build. Hence, the problem is solved in the logarithmic domain of $E(\mathbf{q})$, to make it convex and permit
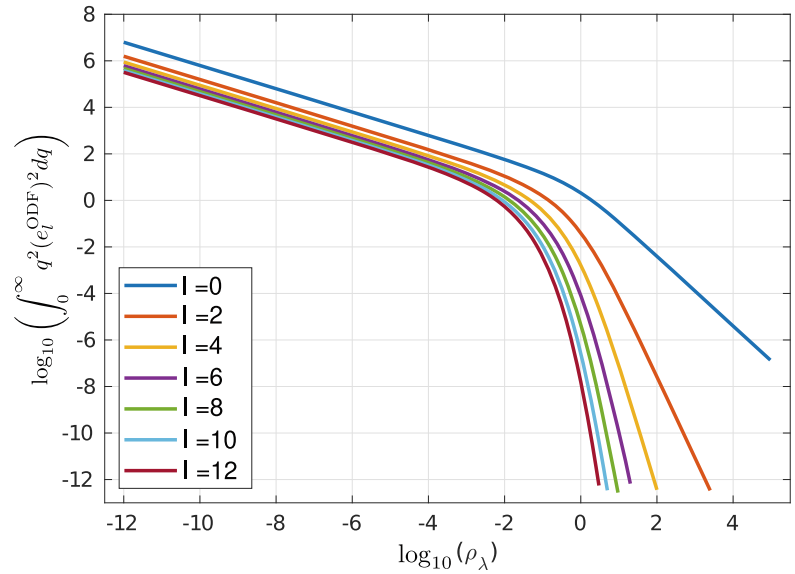
a closed-form solution, while keeping the computationally efficient feature that makes MiSFIT desirable for specific settings. Thus, from now on, our implementation of the *closest* Gaussian propagator will be referred to as "DTI-like propagator." More information about the Gaussian propagator and the method chosen to compute it is included in the Supporting Information Appendix E. We demonstrate in Appendix C that the quotient in Equation (15) equals:

$$\left(\frac{\langle cE(\mathbf{q}), cG(\mathbf{q}, \hat{\mathbf{D}}) \rangle}{\|cE(\mathbf{q})\| \|cG(\mathbf{q}, \hat{\mathbf{D}})\|} \right)^2$$

$$= \frac{\left(\frac{1-f}{\sqrt{|\hat{\mathbf{D}}+\mathbf{D_0}|}} + f\sum_{l,m} \phi_l^m \xi_l^m \right)^2 \sqrt{8|\hat{\mathbf{D}}|}}{(1-f)^2 E_{\text{iso}} + f^2 E_{\text{ani}} + f(1-f) E_{\text{mix}}}, \quad (16)$$

where $\hat{\mathbf{D}}$ is the DTI-like propagator; $\mathbf{D_0} = D_0 I_3$ is D_0 times the identity matrix; $|\cdot|$ stands for the determinant; ξ_l^m are the SH coefficients of a spherical function defined in Supporting Information Appendix C that depends on $\hat{\mathbf{D}}$, $\lambda_\parallel$ and $\lambda_\perp$. Finally, the NG reads:

$$\text{NG} = \sqrt{1 - \frac{\left(\frac{1-f}{\sqrt{|\mathbf{D_0}+\hat{\mathbf{D}}|}} + f\sum_{l,m} \phi_l^m \xi_l^m \right)^2 \sqrt{8|\hat{\mathbf{D}}|}}{\frac{(1-f)^2}{(2D_0)^{3/2}} + f^2 \sum_{l,m} (\phi_l^m)^2 \pi \delta_\lambda^{-3/2} \mathcal{I}_l(\rho_\lambda)}}. \quad (17)$$

Again, evaluating the NG for $f = 1$ yields to a simpler expression:

$$\text{NG} = \sqrt{1 - \left(8\delta_\lambda^3 |\hat{\mathbf{D}}|\right)^{1/2} \frac{\left(\sum_{l,m} \phi_l^m \xi_l^m\right)^2}{\pi \sum_{l,m} (\phi_l^m)^2 \mathcal{I}_l(\rho_\lambda)}}. \quad (18)$$

For values of f other than 0, finding the Gaussian counterpart to the MiSFIT-estimated EAP is not equally easy. This is not an issue within the (anisotropic) MAP-MRI framework, since it represents the diffusion signal as a series of orthogonal cumulants, being the DTI estimation the first one, that is:

$$E_{\text{MAP}}(\mathbf{q}) = E_{\text{DTI}}(\mathbf{q}) + E_{\text{MAP}\backslash\text{DTI}}(\mathbf{q}), \quad (19)$$

so that the closest Gaussian is just the first addend. As already explained in the beginning of the section, MiSFIT can only compute a "DTI-like" propagator in order not to maim its computational efficiency.

3 | METHODS

3.1 | Materials

In vivo validation has been carried out using only publicly available databases:

- The **HCP** (Human Connectome Project)[1]MGH-USC dataset (subject 1007) comprises high-quality DWI volumes acquired on a Siemens 3T Connectome Scanner (Siemens) with maximum gradient strength 300 mT/m.

The data were acquired with a spin-echo echo planar imaging (EPI) with TR/TE = 8000/57 ms, four different shells at b = [1000, 3000, 5000, 10000] s/mm² with [64, 64, 128, 256] diffusion gradients each, and 40 interleaved nonweighted baselines, in-plane resolution 1.5×1.5 mm² and slice thickness 1.5 mm, and pulse separation time/diffusion gradients length $\Delta/\delta =$ 21.8/12.9 ms. The outermost shell has been removed in order to validate our proposal with more standard acquisitions.

- The **MICRA** (Micro-structural Image Compilation with Repeated Acquisitions) database[17] contains five repeated sets of multishell samplings DWI for each of six healthy volunteers. The images were acquired within a 2-week period, approximately at the same time for each participant—avoiding potential diurnal effects—on an ultra-strong gradient 3T Connectome MRI scanner using a single-shot spin echo EPI with TR/TE = 3000/59 ms, six different shells at b = [200, 500, 1200, 2400, 4000, 6000] s/mm², with [20, 20, 30, 61, 61, 61] gradient directions, respectively, in-plane resolution 2×2 mm², slice thickness 2 mm and $\Delta/\delta = 24/7$ ms. The data were preprocessed by removing Gibbs ringing artifacts[18] (with MRtrix3[19]) and correcting susceptibility-induced distortions (with FSL's `topup`; Analysis Group, FMRIB, Oxford, UK.; https://fsl.fmrib.ox.ac.uk/fsl/fslwiki[20,21]) and B1 field inhomogeneity[22] (with MRtrix3).

3.2 | Implementation details

The fitting procedure for parameters f, $\lambda_\parallel$ and $\lambda_\perp$ in Equations (5) and (6), and the computation of the ODF's SH coefficients, is detailed in Reference 16. We have used $L = 8$ as the maximum order for SH expansions, and empirically set $\mu = 1.2 \cdot 10^{-4}$ as the regularization parameter described therein to avoid singular convolution kernels. To compute $\mathcal{I}_l(\rho_\lambda)$, we have resorted to linear interpolation in the logarithmic domain from the values depicted in Figure 1. The whole MiSFIT framework, including the newly introduced PA and NG, was coded in Matlab® R2019b (The MathWorks, Inc.) and is available for download [2].

The computation of PA and NG with MiSFIT is validated by comparing them with the de facto standard in the related literature, that is, the MAPL as described in Reference 4. We have used the implementation in the DIPY package [3] under Python 3, though the actual

code allowing the computation of the PA within the anisotropic MAP-MRI reconstruction was kindly provided by the authors on demand. We use MAPL with positivity constraints and cross-validation for setting the Laplacian penalty term. The maximum order for the basis functions was set to 6.

In both cases, and unless otherwise noticed, both PA and NG have been set up using the entirety of the acquisition's shells.

3.3 | Ground-truth-based evaluation

Numeric comparisons over ground-truth data are based on the methodology originally proposed in Reference 16. A micro-structure model is estimated at representative regions of the WM using NODDI.[23] Afterwards, a statistical model is built upon the estimated parameters, and further used to draw random samples that are fed to the forward NODDI model to generate synthetic samples simulating 1, 2, or 3 crossing fibers at will with a known Peak Signal to Noise Ratio (PSNR). As long as the generative model can be sampled for any gradient direction and b-value, ground-truth values are easily obtained for any dMRI measure with arbitrary precision by numerical integration. See Reference 16 for further details on this methodology. While the ground truth for the PA is somehow trivial via the SH representation, determining the ground truth of NG implies solving a problem of calculus of variations. So this is transformed into a Least Squares optimization one by minimizing the squared residuals of a preset number of **q**-space samples and then solved in the logarithmic domain of $E(\mathbf{q})$, as explained in Section 2.3.

3.4 | Reliability study

The repeated acquisitions within MICRA dataset have been used to assess the repeatability of the computed measures (i.e. intersession variability) and the separability they provide (i.e. intersubject differences). These complementary properties together characterize the reliability of each method (MiSFIT/MAPL) and measure (PA/NG).[24] Note that DTI's FA and DKI's mean Kurtosis have been included in the table for a wider comparison.

The design of the corresponding experiment is as follows: First, ROIs were back-projected by registering the JHU atlas' labels[25] (in MNI152 space) into each subjects' space by means of linear plus nonlinear registration (FSL's[26] FLIRT and FNIRT,[27] respectively) of the subject's FA to the JHU atlas, followed by the application of the inverse warping to the JHU labels. An eroded mask of the
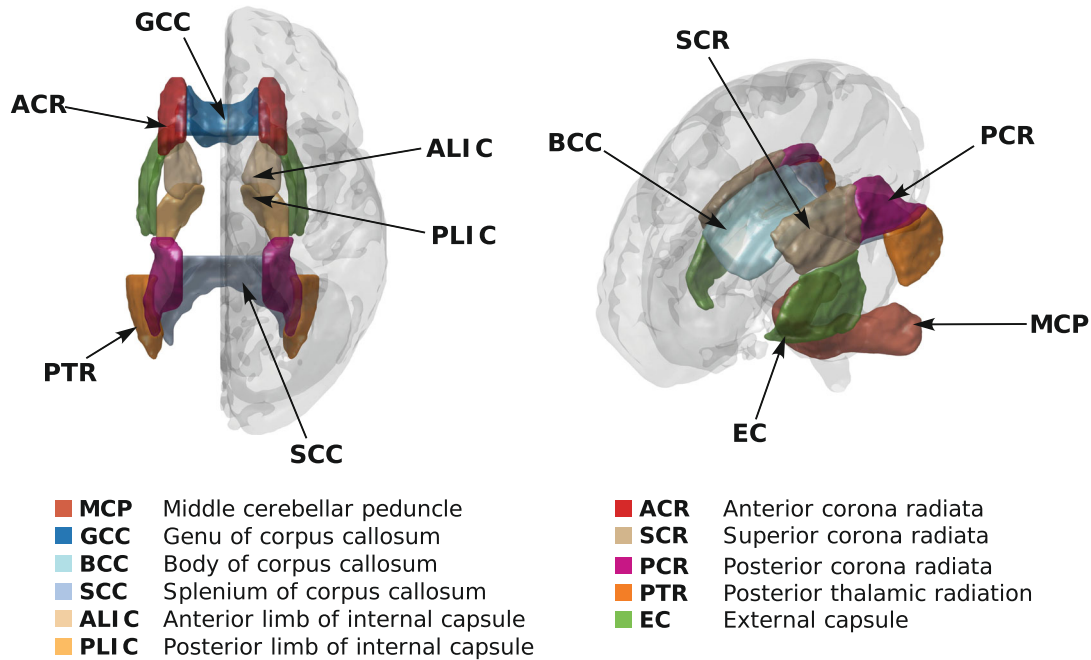
FIGURE 2 Three-dimensional visualization of the 11 JHU DTI-based labels in standard space. Note that some of the regions are not shown in either subfigure, in order to ease the visualization.

regions with a kernel of size $2 \times 2 \times 2$ was then computed to palliate the effects of a possible misalignment in the registration, removing tissue regions potentially affected by a partial volume effect, followed by the removal of those values for which the FA in the region yielded outliers (defined as those values falling 1.5 times outside the interquartile range). More information about the outlier rejection procedure is included in the Supporting Information Appendix E.1. Finally, for each ROI in the subject space, one single-valued representative of each measure was computed as the median value. Figure 2 shows a 3D brain render of the 12 WM regions included in the study (i.e., those in the JHU DTI-based atlas). Note that ROIs in both right and left hemisphere have been merged together into a single region.

Repeatability was then computed as the mean across subjects of the variances across sessions, while separability was computed as the variance across subjects of the means across sessions. A Figure of Merit (FoM) was lastly defined as the separability over repeatability ratio. Owing to the limited size of the database, a 200-runs bootstrap analysis over population's subsets was carried out to assess the confidence we can put on such FoM, expressed as its coefficient of variation (CV):

$$\text{CV}_{\text{FoM}} = \left(1 + \frac{1}{4n}\right)\frac{s}{\bar{x}}, \tag{20}$$

with $\bar{x}/s$ the mean/SD over bootstrapped samples, and n the number of bootstrap samples, used in the first term to attain unbiased estimates of the CV.

3.5 | Computational time evaluation

One main advantage of MiSFIT, as compared to MAP-MRI/MAPL, is its computational efficiency, which allows to estimate the EAP two orders of magnitude faster. Nonetheless, the computation of scalar measures from the reconstructed EAP can result in nonnegligible computational overloads: while the computation of NG is straightforward after the non-isotropic MAP-MRI signal representation, this is not the case for PA, which requires nontrivial extra calculations.

For this reason, it makes sense to compare how long MiSFIT and MAPL take to compute (1) the signal representation, (2) the PA and (3) the NG. The experiment is carried out with the aforementioned Matlab's (for MiSFIT) and Python DIPY's (for MAPL) implementations running in a quad-core Intel © CoreTM i7-6500U processor with 8GB RAM.

4 | RESULTS

4.1 | Visual assessment

Figures 3 and 4 compare the computations of PA and NG by MiSFIT and MAPL for the randomly chosen third session of the fourth MICRA's subject. With regard to PA, MAPL presents a noisier behavior (Fig. 3, left), specially in those areas with lower anisotropy values —except the ventricles, which MiSFIT clearly fails to delineate. This can
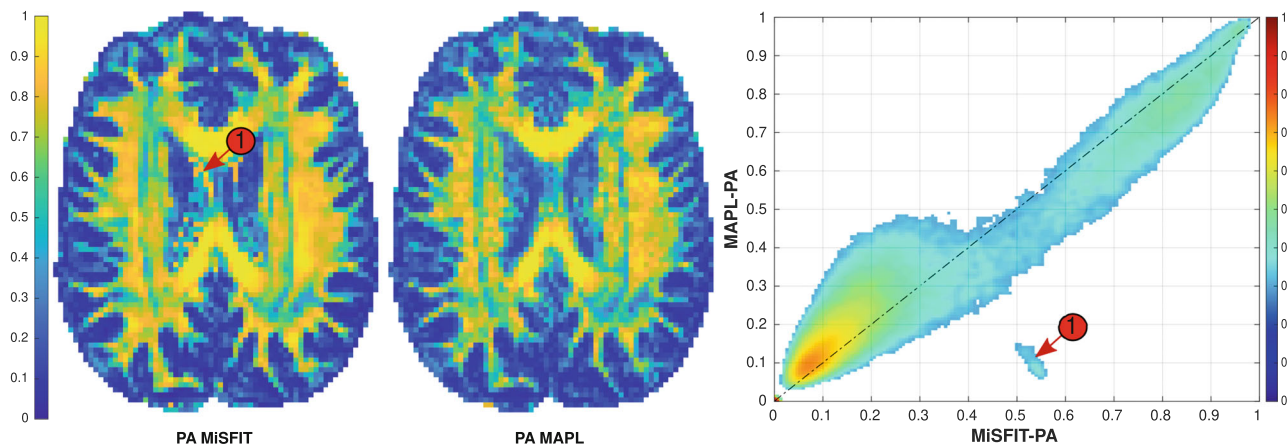
FIGURE 3 Comparison of the PA maps obtained with either MiSFIT and MAPL for the third session of the fourth MICRA's subject. Left: visual assessment within the whole range of variation [0, 1]. Right: joint 2-D histograms (logarithmic) of MAPL's values vs. MiSFIT's. The high-valued islands within MiSFIT (tag numbered '1') correspond to ambiguous configurations of the convolutional representation of MiSFIT.
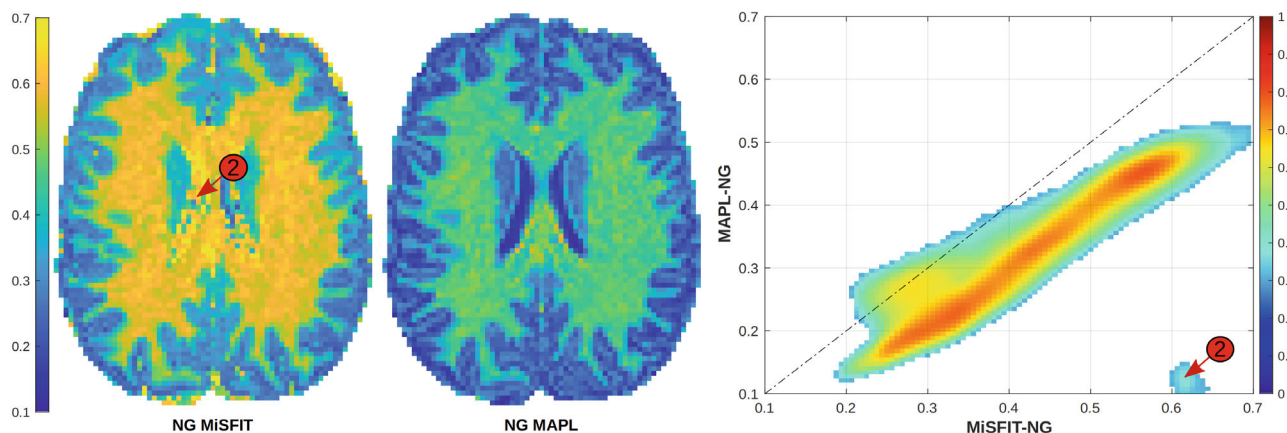

FIGURE 4 Comparison of the NG maps obtained with either MiSFIT and MAPL for the third session of the fourth MICRA's subject. Left: visual assessment within the cropped range [0.1, 0.7]. Right: joint 2-D histograms (logarithmic) of MAPL's values vs. MiSFIT's. The outliers tagged with '2' correspond to ambiguous configurations of the convolutional representation of MiSFIT.

also be observed in areas with higher anisotropy, resulting, for example, in some visible discontinuities in the *external capsule*. In comparison, MiSFIT produces a more saturated map, clearly defining the major WM fiber tracts and their limits, making even more distinguishable the anisotropy of diffusion processes in some brain regions. Nonetheless, this contrast saturation does not imply, *per se*, a more accurate result. The comparison can also be analysed in terms of the two-dimensional (2D) joint histogram (Figure 3, right), which shows a linear correlation between both metrics, only disturbed for lower PA values, where the histogram broadens. As explained in Reference 16, MiSFIT's estimation produces artifacts (tagged with number 1) due to ambiguities in highly isotropic zones (such as the ventricles or the gray matter), where the optimizer has to decide, in Equations (5) and (6), whether $f = 1$ or $\lambda_\perp \simeq \lambda_\parallel$.

For NG, both MiSFIT and MAPL provide outcomes as similar as those found with PA (Figure 4, left), with the exception of the overall negative bias MAPL introduces w.r.t MiSFIT. This shift is more clearly visible in Fig. 4, right: MAPL's values are strongly linearly correlated with MiSFIT's, but placed along a line with slope less than 1 and negative bias. Once again, MiSFIT fails to delineate the ventricles due to the ambiguity in the representation, yielding to the outlier tagged as 2 in the histogram.

4.2 | Quantitative analysis based on ground-truth

The numerical assessment of the accuracy of each method is based on the ground-truth data described in Section 3.3: Figures 5 and 6 show the similarity of PA and NG, as
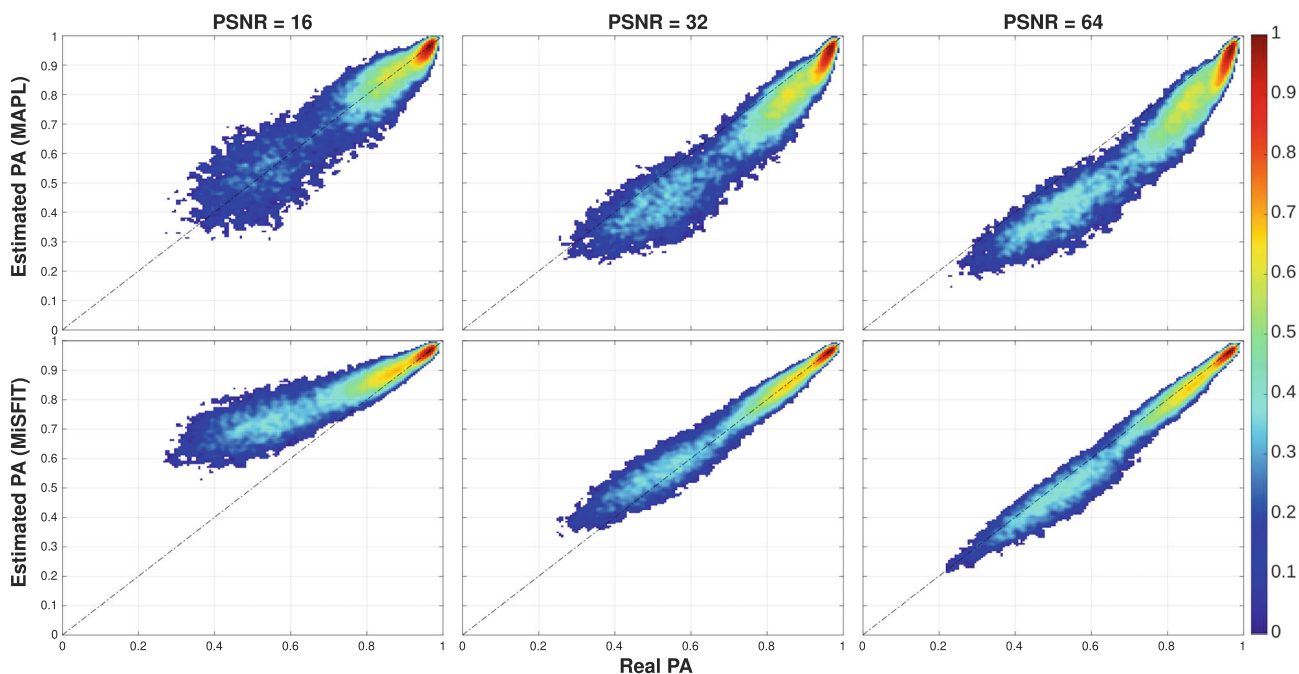
FIGURE 5 Two-dimensional joint histogram of the estimated propagator anisotropy (*y*-axis) against synthetic ground truth values (*x*-axis) for different peak signal to noise ratio (PSNR, 16 left, 32 middle, 64 right). There exists a significant linear correlation between the estimated and real values, with micro-structure adaptive convolution kernels and dual Fourier integral transforms being clearly more accurate and less variable than MAPL for PSNR > 32.
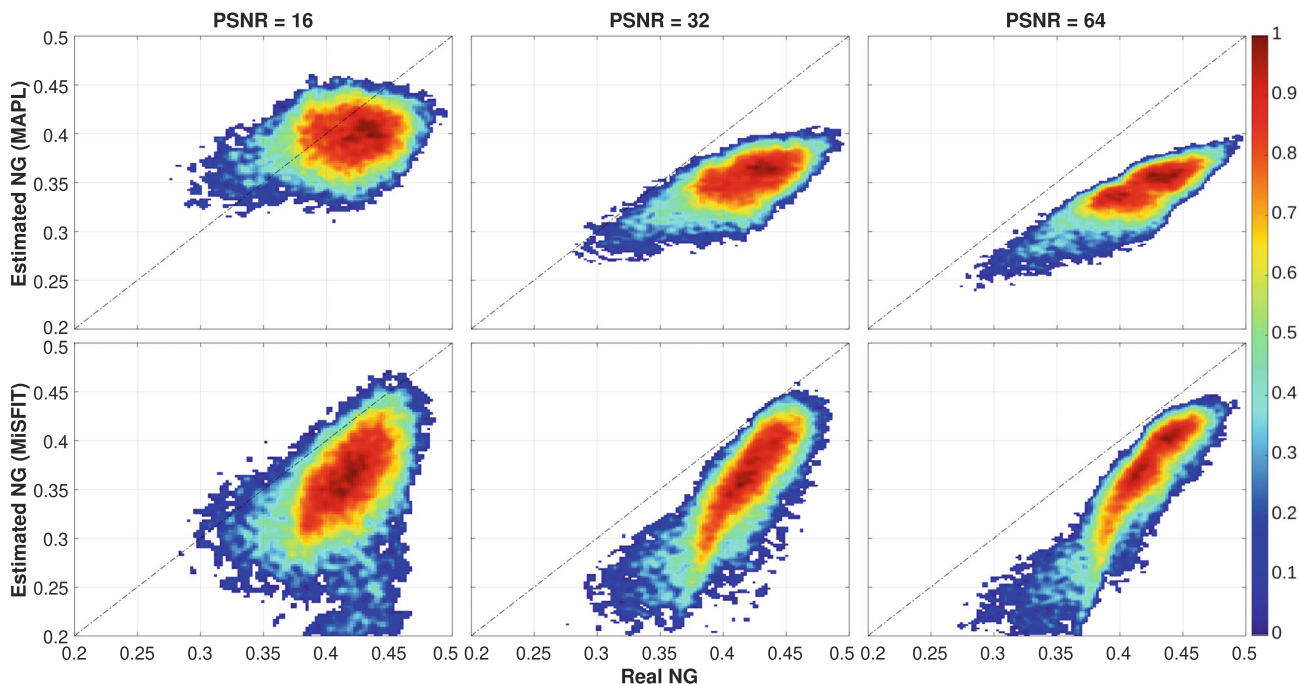

FIGURE 6 Two-dimensional joint histogram of the estimated non-Gaussianity (*y*-axis) against synthetic ground truth values (*x*-axis) for different peak signal to noise ratio (PSNR, 16 left, 32 middle, 64 right). A linear correlation can be appreciated in both PSNR = 64 maps. Micro-structure adaptive convolution kernels and dual Fourier integral transforms tends to be more accurate in the high values, while MAPL estimation gets unbiased for lower ones, as well as for PSNR = 16.
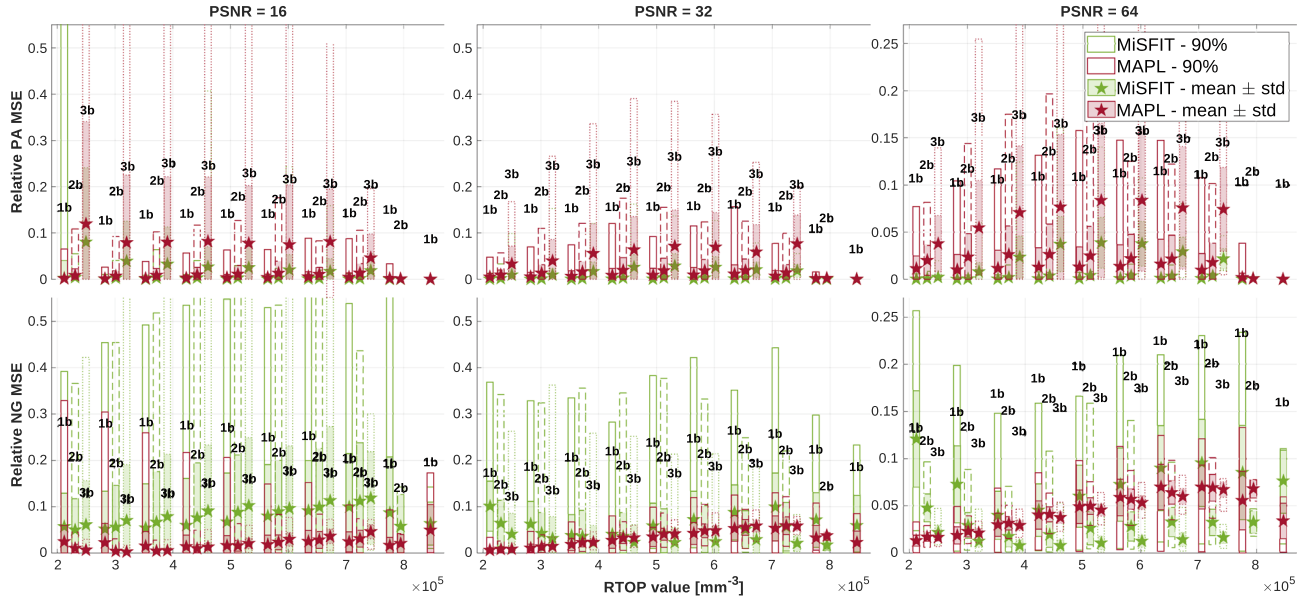
FIGURE 7 Estimated relative mean squared error (rMSE) of propagator anisotropy (PA) (top) and non-Gaussianity (NG) (bottom) as a function of signal's bandwidth (i.e. RTOP), for different peak signal to noise ratio (16 left, 32 middle and 64 right) and 1, 2 or 3 fiber crossing configuration. Missing bars correspond to those fiber bundle configurations for which PA, NG or RTOP values could not be computed. Statistical properties displayed: mean (star-shaped symbol), SD (full-colored box), 90% confidence interval (empty box).

computed with each of MAPL and MiSFIT, with true values of PA and NG, respectively. Joint 2D histograms have been computed for different PSNR values (16, 32, and 64). Figure 7 shows the rMSE for PA and NG estimates from both MAPL and MiSFIT as a function of the ground-truth RTOP value, as in Reference 16. This choice is based on the definition of RTOP as the integral of the attenuation signal in the whole **q**-space:

$$\text{RTOP} = \int_{\mathbb{R}^3} |E(\mathbf{q})|^2 d\mathbf{q}, \qquad (21)$$

which directly relates RTOP to the bandwidth of the EAP.

For PSNR = 64, MiSFIT results in more accurate **PA** maps than MAPL from every possible point of view: Not only depicting smaller variability across the dynamic range, but also resulting in mean values closer to the ground truth. When conditions worsen, for example, PSNR = 16, MiSFIT obtains poorer results, overestimating the anisotropy in highly isotropic regions. These PA estimates, however, get more accurate the more anisotropic the region is.

Regarding the relative MSE (top of Figure 7), MiSFIT yields to smaller errors, constantly outperforming MAPL values for any given bandwidth, PSNR or fiber bundle configuration. This latter variable is responsible of the poorer behavior of MiSFIT in Figure 5 with PSNR = 16. Arguably, both PA estimates worsen as the number of crossing fibers increases, which may be caused by the representation's difficulties when computing the isotropic EAP

counterpart from bundles that may have different diffusion properties. Notice that, despite the results being worse for the third bundle configuration, they still outperform MAPL's.

The discussion for the NG is not equally good to MiSFIT. Firstly, the two left-most columns of Figure 6 (PSNR 16 and 32, respectively) show bigger variability across the measure's dynamic range, even for those values with means closer to the ground truth than those reported by MAPL. With respect to MiSFIT, there are multiple sources of error that end up stacking one to each other, the main one is driven by the noise—which causes the metric to be underestimated, specially in regions with high-Gaussianity behavior—but also by the estimated EAP—which affects the non-Gaussian regions estimates—and the DTI-estimated equivalent Gaussian EAP—which is greatly palliated as the fiber crossings increases.

On the other hand, the rMSE depicted from MiSFIT's NG (bottom of Figure 7) seems to be dominated by the EAP reconstruction error, which results in MiSFIT underestimating the NG. This behavior is consistent with the one explained in Reference 16 (Figure 8). Interestingly, the rMSE increases when dealing with single-fiber configurations. This may be caused by MiSFIT's construction: The convolution of the Gaussian kernel with a very prolate but not-completely-sampled ODF (i.e. possibly non-Gaussian) results in Gaussian-like distributions, which yields to underestimated NG results. Alternatively, when adding fibers onto the configuration, the reconstructed EAP

function gets smoother over the surface of the sphere, thus getting more accurately defined by the sampling scheme, which in turn leads to more precise estimations of the original EAP. This can also be appreciated in the bottom of Figure 7.

In order to relate the numerically obtained results with in vivo images, the PSNR has been computed for a subject of the MICRA dataset by dividing the filtered (denoised) image by the estimated noise level. Both filtered image and noise level have been computed by using dwidenoise (MRtrix3, Tournier et al., NeuroImage, 2019) on the raw images. Finally, a WM mask has been crafted by merging all the (previously eroded) JHU WM labels. The resulting PSNR is 28.12, a usual result for good-quality acquisitions such as MICRA. This result indicates that the in vivo images in Figures 2 and 3 (from MICRA dataset) can be related to the middle column in Figures 4, 5, and 6. In this PSNR range, the MiSFIT's PA portrays a much less variable estimation than MAPL's. MiSFIT tends to overestimate the mid-low PA values, while MAPL tends to subestimate them. MiSFIT's RMSE depicts a better accuracy in either bundle configuration and throughout the entire bandwidth range. Regarding the NG, the variance of the estimation increases significantly, yielding to subestimated results for both MiSFIT and MAPL. Concerning the RMSE, for the lower bandwidth ranges the MiSFIT's NG results in slightly less accurate estimations, which are improved in the mid-to-high bandwidth ranges.

4.3 | Reliability study

The results corresponding to the experiment described in Section 3.4 are summarized in Tables 1 and 2. Table 1 reports the FoM—the reliability measurement—together with the CV of the repeatability values. Table 2 shows the FOM's bootstrapped CV.

The first thing to notice from Table 1 is that all FoM values are greater than one, meaning that, for any given ROI, the intersubject variability of the metrics is greater than the intrasubject variability. Regarding the PA, both MiSFIT and MAPL exhibit the same tendency, yielding to reliability values in the same order of magnitude, with the exception of the GCC where MAPL depicts much greater results than MiSFIT, and the external capsule where MiSFIT depicts greater results than MAPL. The reliability of the MiSFIT's NG, on the other hand, outperforms MAPL in most regions, for example in the three subregions of the *corpus callosum* (CC)—*genu*, *body*, and *splenium*—which together form one of the biggest connective pathways in the brain.

In terms of repeatability, both measures result in stable outputs throughout the various sessions of a given subject, yielding low CV values. MAPL's PA results in more repeatable values in 6 out of 11 regions while giving virtually equal values for two of the rest (BCC and PLIC, with less than 10% difference between both frameworks); whereas MAPL's NG depicts higher repeatability in 5 out of the 11 regions. To widen the comparison with existing

T A B L E 1　Repeatability coefficient of variation (‰) over reliability (FoM) values for each of the regions, measures (PA, NG) and methods (MiSFIT, MAPL)

Region	PA		FA	NG		MK
	MAPL	MiSFIT	DTI	MAPL	MiSFIT	DKI
MCP	0.113 / 3.54	0.064 / 2.09	0.184 / 2.64	0.035 / 2.66	0.136 / 3.82	0.039 / 1.44
GCC	0.067 / 13.49	0.151 / 4.59	0.192 / 13.20	0.120 / 3.59	0.070 / 19.74	0.072 / 8.58
BCC	0.057 / 4.66	0.061 / 4.31	0.077 / 7.42	0.087 / 1.98	0.016 / 4.37	0.010 / 11.83
SCC	0.006 / 14.7	0.026 / 10.86	0.018 / 33.42	0.049 / 5.77	0.003 / 40.94	0.025 / 17.46
ALIC	0.078 / 3.04	0.148 / 5.25	0.149 / 2.57	0.056 / 4.00	0.045 / 1.40	0.035 / 13.01
PLIC	0.045 / 6.55	0.049 / 3.72	0.059 / 7.07	0.030 / 3.31	0.015 / 8.43	0.021 / 9.43
ACR	0.152 / 3.42	0.024 / 3.39	0.033 / 11.33	0.026 / 4.55	0.036 / 14.30	0.024 / 14.37
SCR	0.232 / 3.38	0.019 / 3.21	0.067 / 24.30	0.023 / 2.26	0.040 / 35.15	0.017 / 5.32
PCR	0.157 / 3.14	0.034 / 2.00	0.349 / 1.20	0.021 / 2.34	0.152 / 2.12	0.037 / 6.70
PTR	0.192 / 5.05	0.023 / 5.98	0.252 / 2.06	0.036 / 3.42	0.083 / 2.03	0.016 / 18.82
External capsule	0.729 / 3.39	0.035 / 17.30	0.352 / 5.35	0.075 / 7.1	0.491 / 5.47	0.022 / 18.84

Notes: DTI's FA and DKI's MK have been added for a wider comparison. Results indicate a good ratio between inter-subject and the intra-subject variability for both measures. On average, MiSFIT's NG obtain slightly better results than MAPL's, for example, in the *corpus callosum*, while resulting in less reliable PA maps than those obtained with MAPL or DTI's FA.

Abbreviations: FA, Fractional Anisotropy; MiSFIT, micro-structure adaptive convolution kernels and dual Fourier integral transforms; NG, non-Gaussianity; PA, Propagator Anisotropy.

TABLE 2 Bootstrap-derived CV of the FoM values for each of the regions, measures (PA, NG) and methods (MiSFIT, MAPL), together with the DTI's FA and the DKI's MK, for a wider comparison

| Region | PA | | FA | NG | | MK |
	MAPL	MiSFIT	DTI	MAPL	MiSFIT	DKI
MCP	0.596	0.658	0.613	0.494	0.225	0.325
GCC	0.385	0.230	0.243	0.318	0.303	0.199
BCC	0.524	0.557	0.588	0.310	0.408	0.437
SCC	0.488	0.431	0.516	0.324	0.293	0.486
ALIC	0.331	0.368	0.332	0.351	0.322	0.322
PLIC	0.719	0.399	0.553	0.409	0.342	0.203
ACR	0.359	0.275	0.416	0.488	0.649	0.323
SCR	0.679	0.522	0.491	0.502	0.488	0.430
PCR	0.256	0.559	0.334	0.378	0.382	0.326
PTR	0.170	0.304	0.333	0.388	0.513	0.586
External capsule	0.659	0.328	0.276	0.305	0.326	0.201

Note: The bootstrap was computed by doing 200 runs.

Abbreviations: FA, Fractional Anisotropy; FoM, Figure of Merit; MiSFIT, micro-structure adaptive convolution kernels and dual Fourier integral transforms; NG, non-Gaussianity; PA, Propagator Anisotropy.

and previously validated measures, the table also includes the reliability and repeatability values for FA and MK (mean Kurtosis) from DTI and DKI frameworks, respectively. As it can be seen, the FA shows the same tendency to that of MAPL and MiSFIT, with the only exceptions being ACR and SCR. Concerning the MK, which outperforms both MAPL and MiSFIT's reliability values in six of the regions, it is worth noticing that this measure is not as similar to the NG as the FA is to the PA. That is simply because, by definition, the mean Kurtosis is computed as the mean of individual kurtoses calculated along all gradient directions, whereas NG requires the three-dimensional EAP and its three-dimensional Gaussian counterpart to compute the dissimilarity of the projection onto a multi-dimensional vector; thus being affected by moments with order higher than kurtosis.

The results shown in the previous table are supplemented by the bootstrap-derived coefficients of variation of the reliability values in Table 2, which gives us insights about the reliability of the FoM values. For example, we can conclude that repeated acquisitions of the FoM value for the MAPL's PA in the *middle cerebellar peduncle* (MCP, 2.09) yield to variations 0.658 times its mean, thereby making us aware of the variation of such value, and able to question its trustworthiness.

4.4 | Computational time evaluation

Arguably, one notorious factor that conditions the actual clinical applicability of EAP imaging resides in the computational time requirements. Table 3 shows the time needed

TABLE 3 Time consumption on the different phases of the metric's computation. Fitting the MAPL model is three-orders of magnitude more time-expensive than MiSFIT

Phases	MAPL	MiSFIT
Fit Model	8 h 36 min	17 s
PA Computation	2 h 19 min	1 s
NG Computation	3 s	6 s
Total time	10 h 56 min	23 s

Note: MAPL requires almost 11 h for a single DWI volume, in comparison with MiSFIT's 23 s, which makes the former unfeasible for clinical applicability.

Abbreviations: FA, Fractional Anisotropy; MiSFIT, micro-structure adaptive convolution kernels and dual Fourier integral transforms; NG, non-Gaussianity; PA, Propagator Anisotropy.

by MiSFIT and MAPL to (1) fit the signal, (2) compute the PA, and (3) compute the NG. As it can be seen, fitting the signal to MAPL requires almost 9 h for a single DWI MICRA volume with size (110, 110, 66, 266). MiSFIT does so in less than 20 s.

As expected, the PA computation is time-consuming for the MAPL approach, which has to recalculate the MAP-MRI isotropic coefficients from those of the anisotropic representation. MiSFIT, on the contrary, only has to take the first SH coefficient to estimate the isotropic counterpart. This process ends up taking MAPL 2 h 20 min in comparison with MiSFIT's 0.345 s.

Finally, the NG is easily computed by MAPL, which only has to take the first coefficient (Gaussian) from its series expansion and compute the angular divergence. In

this case, MAPL computes the measure in 3.6 s while MiSFIT takes 5.8 s.

To sum up, the total time required by either framework to actually produce a meaningful map is no less than 8 h 30 min for MAPL (fit the model and compute the NG) compared with MiSFIT's maximum of 22 s (fit the model and compute the NG). Needless to say, this time-consuming difference is of main importance not only in clinical settings, but also in the processing of large data sets that are becoming more common in the dMRI community.

5 | DISCUSSION

In this paper we have shown how two descriptors of the WM anatomy, PA and NG, can be computed within MiSFIT with very little computational effort. This way, we have generalized the analysis described in the original work,[16] based on raw moments, to normalized indices that can be easier to interpret.

Regarding the PA, we have shown that MiSFIT yields to maps comparable to those obtained with MAPL. Yet, according to the numerical simulations, MiSFIT results are more accurate. This remains true in regions with diverse anisotropic behavior, and becomes compromised only when dealing with attenuation signals highly contaminated by noise. The reliability evaluation depicts comparable outcomes for both frameworks; meaning that, in general, none is far superior than the other and result, on average, in estimates almost identical (5.85 for MAPL, 5.70 for MiSFIT). In some particular regions, however, substantial differences can be found. The repeatability assessment, on the other hand, yields to MiSFIT estimates more repeatable than MAPL's (on average, 0.06 and 0.17%0, respectively). Thus, we conclude not only that MiSFIT's PA leads to a desirable stability of measurements throughout the sessions (in its maximum, the average subject's measures of the GCC varies 0.151%0 its mean), but also that its reliability is comparable to that of MAPL.

Concerning the NG, we have shown the high correlation between MiSFIT's and MAPL's estimates, disturbed only by MiSFIT's noisier behavior in Gaussian regions. Overall, MiSFIT exhibits a positive bias compared to MAPL for all the range of NG. According to the numerical simulations in Figure 6, however, both frameworks clearly underestimate the *actual* value of the NG. Paradoxically, the negative bias in MAPL increases with the PSNR. Yet, the (negative) bias introduced by MiSFIT is less severe than MAPL's, which is consistent with the experiment in Figure 4 with real data. Therefore, the large relative errors reported in Figure 7 for the NG (far larger than those for the PA) are likely explained by the bias in the estimation. Similar to PA, both frameworks depict highly repeatable

results across intra-subject sessions (0.05%0 for MAPL, 0.10%0 for MiSFIT, averaging across regions). In terms of reliability, MiSFIT's estimates are, on average, far more reliable (12.52 against MAPL's 3.73).

Note the evaluation of the NG based on ground-truth is far more difficult than it is for the PA, since the definition of the NG is tightly related to the MAP-MRI representation: with MAP-MRI, the closest Gaussian is trivially computed as the first addend of the expansion, so that the non-Gaussian part of the EAP is orthogonal to its Gaussian part. This property is unique to MAP-MRI, and does not hold neither for MiSFIT nor for the designed ground-truth signal. Consequently, it remains unclear if our ground truth is actually the desirable target. Given this situation, the reliability analysis grants a valuable quantitative information without the need of a ground-truth. In this sense, MiSFIT outperforms MAPL's estimation of the NG in 7 out of the 11 regions studied, including the CC. Taking also into account that MiSFIT offers a higher dynamic range for the NG, see Figure 4 (left), we postulate that MiSFIT can be an attractive alternative to compute this index.

The numerical validation based on reliability, not just repeatability, is indeed a novel contribution of the present paper, as separability is a desirable property for any anatomical index. We claim that assessing the reliability is mandatory when comparing different dMRI techniques since EAP imaging approaches crop the otherwise infinite bandwidth of the diffusion signal in different ways (see Reference 16), depending on the representation used. The main limitation of the reliability assessment is the need for a robust intersubject registration, so that the registration error does not become a critical confounding factor. In this sense, the repeatability values added to the analysis together with the computation of bootstrapped FoMs in Table 2 gives an idea of the confidence we can put on the results in Table 1. As long as the coefficients of variation are relatively large in all cases, we may conclude that more work is needed to pose the assessment of reliability as a state of the art procedure.

A critical issue with previous implementations of both the PA and the NG is their time-consuming nature, unsuited for clinical practice. According to Table 3, the time required for processing an entire volume of the MICRA database with MAPL is well over 8 hours when Generalized Cross-validation and Positivity Constraints are used. For a subject in the HCP database, this time can grow up to 52 h. Provided that for a clinical study a whole database needs to be processed, researchers will be compelled to use sub-optimal configurations, without positivity constraints, with fixed Laplacian penalty terms, or cropping the maximum order of the basis functions, which will compromise the accuracy of the measures

and, in turn, the quality of the study. MiSFIT, on the other hand, is two orders of magnitude faster for any configuration.

To sum up, in this work the PA and NG measures have been introduced, their equations derived for MiS-FIT's full composite attenuation signal and their performance within such framework validated. Both measures, with several proven clinical applications, result in consistent and reliable maps. All of this, together with MiSFIT's proven efficiency—capable of modeling the signal and computing both maps in less than a minute compared to MAPL's 11 h—make the MiSFIT framework qualified for the new standardized dMRI protocol within clinical settings.

CONFLICT OF INTEREST

The authors declare that there is no conflict of interest.

ORCID

Guillem París https://orcid.org/0000-0002-1564-1199
Tomasz Pieciak https://orcid.org/0000-0002-7543-3658
Santiago Aja-Fernández https://orcid.org/0000-0002-5337-5071
Antonio Tristán-Vega https://orcid.org/0000-0002-4614-2501

REFERENCES

1. Novikov DS, Kiselev VG, Jespersen SN. On modeling. *Magnetic Resonance in Medicine*. 2018;79:3172-3193.
2. Callaghan PT. *Principles of Nuclear Magnetic Resonance Microscopy*. Clarendon Press; 1991.
3. Wu YC, Alexander AL. Hybrid diffusion imaging. *NeuroImage*. 2007;36:617-629.
4. Fick RH, Wassermann D, Caruyer E, Deriche R. MAPL: tissue microstructure estimation using Laplacian-regularized MAP-MRI and its application to HCP data. *NeuroImage*. 2016;134:365-385.
5. Ning L, Westin CF, Rathi Y. Estimating diffusion propagator and its moments using directional radial basis functions. *IEEE Trans Med Imaging*. 2015;34:2058-2078.
6. Özarslan E, Koay CG, Shepherd TM, et al. Mean apparent propagator (MAP) MRI: a novel diffusion imaging method for mapping tissue microstructure. *NeuroImage*. 2013;78: 16-32.
7. Galazzo IB, Brusini L, Obertino S, Zucchelli M, Granziera C, Menegaz G. On the viability of diffusion MRI-based microstructural biomarkers in ischemic stroke. *Front Neurosci*. 2018; 12:92.
8. Avram AV, Sarlls JE, Barnett AS, et al. Clinical feasibility of using mean apparent propagator (MAP) MRI to characterize brain tissue microstructure. *NeuroImage*. 2016;127: 422-434.
9. Kraus MF, Susmaras T, Caughlin BP, Walker CJ, Sweeney JA, Little DM. White matter integrity and cognition in chronic traumatic brain injury: a diffusion tensor imaging study. *Brain*. 2007;130:2508-2519.
10. Barnea-Goraly N, Kwon H, Menon V, Eliez S, Lotspeich L, Reiss AL. White matter structure in autism: preliminary evidence from diffusion tensor imaging. *Biolog Psych*. 2004;55:323-326.
11. Fick RHJ, Daianu M, Pizzolato M, et al. Comparison of biomarkers in transgenic Alzheimer rats using multi-shell diffusion MRI. In: Fuster A, Ghosh A, Kaden E, Rathi Y, Reisert M, eds. *Computational Diffusion MRI. MICCAI 2016. Mathematics and Visualization.* Springer; 2017:187-199.
12. Wang P, Weng L, Xie S, et al. Primary application of mean apparent propagator-MRI diffusion model in the grading of diffuse Glioma. *Eur J Radiol*. 2021;138:109622.
13. Song SK, Yoshino J, Le TQ, et al. Demyelination increases radial diffusivity in corpus callosum of mouse brain. *NeuroImage*. 2005;26:132-140.
14. Jansen JF, Stambuk HE, Koutcher JA, Shukla-Dave A. Non-Gaussian analysis of diffusion-weighted MR imaging in head and neck squamous cell carcinoma: a feasibility study. *Am J Neuroradiol*. 2010;31:741-748.
15. Yuan J, Yeung DKW, Mok GS, et al. Non-Gaussian analysis of diffusion weighted imaging in head and neck at 3T: a pilot study in patients with nasopharyngeal carcinoma. *PLoS One*. 2014;9:e87024.
16. Tristán-Vega A, Aja-Fernández S. Efficient and accurate EAP imaging from multi-shell dMRI with micro-structure adaptive

convolution kernels and dual Fourier integral transforms (MiS-FIT). *NeuroImage*. 2021;227:117616.

17. Koller K, Rudrapatna U, Chamberland M, et al. MICRA: microstructural image compilation with repeated acquisitions. *NeuroImage*. 2021;225:117406.

18. Kellner E, Dhital B, Kiselev VG, Reisert M. Gibbs-ringing artifact removal based on local subvoxel-shifts. *Magn Reson Med*. 2016;76:1574-1581.

19. Tournier JD, Smith R, Raffelt D, et al. MRtrix3: a fast, flexible and open software framework for medical image processing and visualisation. *Neuroimage*. 2019;202:116137.

20. Andersson JL, Skare S, Ashburner J. How to correct susceptibility distortions in spin-echo echo-planar images: application to diffusion tensor imaging. *Neuroimage*. 2003;20:870-888.

21. Smith SM, Jenkinson M, Woolrich MW, et al. Advances in functional and structural MR image analysis and implementation as FSL. *Neuroimage*. 2004;23:S208-S219.

22. Zhang Y, Brady M, Smith S. Segmentation of brain MR images through a hidden markov random field model and the expectation-maximization algorithm. *IEEE Trans Med Imaging*. 2001;20:45-57.

23. Zhang H, Schneider T, Wheeler-Kingshott CA, Alexander DC. NODDI: practical in vivo neurite orientation dispersion and density imaging of the human brain. *NeuroImage*. 2012;61:1000-1016.

24. Zuo XN, Xu T, Milham MP. Harnessing reliability for neuroscience research. *Nature Human Behav*. 2019;3:768-771.

25. Mori S, Oishi K, Jiang H, et al. Stereotaxic white matter atlas based on diffusion tensor imaging in an icbm template. *Neuroimage*. 2008;40:570-582.

26. Jenkinson M, Smith S. A global optimisation method for robust affine registration of brain images. *Medical image analysis*. 2001;5:143-156.

27. Jenkinson M, Bannister P, Brady M, Smith S. Improved optimization for the robust and accurate linear registration and motion correction of brain images. *Neuroimage*. 2002;17:825-841.

SUPPORTING INFORMATION

Additional supporting information may be found in the online version of the article at the publisher's website.

Appendix A: Legendre Polynomials Integration
Appendix B: Propagator Anisotropy For Eap Composite Signal
Appendix C: Non-Gaussianity For Eap Composite Signal
Appendix D: Efficient Sampling Of Spherical Function
Appendix E: Other Results